Power-scaling of nonlinear-mirror modelocked thin-disk lasers

IVAN J. GRAUMANN,[1] **FRANCESCO SALTARELLI,**[1] **LUKAS LANG,**[1] **VALENTIN J. WITTWER,**[2] **THOMAS SÜDMEYER,**[2] **CHRISTOPHER R. PHILLIPS**[1] **AND URSULA KELLER**[1]

[1]*Institute for Quantum Electronics, ETH Zurich, 8093 Zurich, Switzerland*
[2]*Laboratoire Temps-Fréquence, Université de Neuchâtel 2000 Neuchâtel, Switzerland*
*[*]*ivangr@phys.ethz.ch*

Abstract: We present a first power-scaled nonlinear-mirror (NLM) modelocked thin-disk laser based on an Yb-doped gain material. The laser oscillator delivers average output powers up to 87 W and peak powers up to 14.7 MW with sub-600-femtosecond pulses at ≈9-MHz repetition rate. We demonstrate a threefold improvement in average output power and sixfold improvement in pulse energy compared to previous NLM-modelocking results. We obtain peak powers in excess of 10 MW for the first time from an NLM-modelocked laser oscillator. In our laser, the NLM is assisted by a semiconductor saturable absorber mirror (SESAM) to reliably initiate pulsed operation. We validate the high-power suitability of the NLM modelocking technique using low-absorption $\chi^{(2)}$ crystals and optimized dichroic-mirror coating designs. Furthermore, we discuss stability against Q-switching and study how the tuning of the nonlinear mirror affects the laser performance.

1. Introduction

Ultrafast laser sources are key technological devices to a variety of applications both in industry and scientific research. For example, the combination of high peak power and ultrashort pulse duration has enabled industrial micro-machining, nonlinear biomedical imaging, and frequency conversion to extreme wavelengths such as the extreme ultraviolet (XUV) and THz [1–4]. The development of Yb-based systems, with low-cost direct diode-pumping schemes, further facilitated the deployment of these sources and provided the technology for combining high-power and ultrafast laser operation. Today, the leading technologies for high-power ultrafast laser amplifier systems, namely fiber, slab and thin-disk, are based on a geometry that optimizes the surface-to-volume ratio for efficient heat removal, enabling kW-level average powers [5–8]. These benchmark performances are achieved in amplifier systems which consist of a low-power seed oscillator followed by pulse shaping stages, several amplification stages and compression. Besides the overall large footprint of these multiple stages, high-power amplifiers generally have various trade-offs in terms of beam quality, nonlinearity management, repetition rate scaling, spectral bandwidth, pulse quality, and pulse contrast. Alternatively, high-power ultrafast laser operation can be achieved from a single modelocked laser oscillator combining diffraction-limited beam quality, transform-limited pulses, megahertz repetition rates, and low noise [9]. The thin-disk geometry is well-suited for this purpose, with the thin gain medium providing excellent heat removal capabilities, low nonlinearity and power-scalability [10]. Based on the high quality and technological maturity of Yb:YAG as gain material, thin-disk laser (TDL) oscillators have demonstrated continuous-wave (cw) operation up to 10 kW ($M^2 \approx 10$) from a single disk [11] and ultrafast operation up to 350 W [12].

Ultrafast laser operation in TDL oscillators is achieved via passive modelocking and requires an intracavity saturable loss to initiate and stabilize the pulse formation with soliton modelocking [13,14]. The record performance of 350 W [12] was achieved using a semiconductor saturable

absorber mirror (SESAM) [15] (Fig. 1(a)). The SESAM consists of semiconductor layers forming a distributed Bragg-reflector topped by InGaAs quantum wells acting as saturable absorbers and a top coating for a high damage threshold [15–17]. The epitaxially-grown SESAM structure can be contacted onto a heatsink and directly placed inside the laser resonator to initiate and stabilize soliton modelocking [13]. This flexibility is reflected in the numerous results achieved with very diverse laser configurations and gain materials [9]. However, for targeting shorter pulses, a trade-off between gain bandwidth and average power has been observed for Yb-doped thin-disk gain media when using alternative host materials with broader bandwidths than YAG (see Fig. 3 in [9]). This trade-off is attributed to a combination of less favorable material properties and crystal quality for high-power laser operation, and the slow saturable absorber behavior of the SESAM. Alternatively Kerr-lens modelocked (KLM) thin disk lasers have demonstrated high output powers up to 270 W with 330-fs pulses [18] and 155 W with 140-fs pulses [19] (Fig. 1(a)). Relying on Kerr-lensing combined with soft- and hard-aperture effects, this modelocking scheme provides a fast absorption-free loss modulation. For a given gain material, KLM has enabled shorter pulse durations due to its fast saturable loss mechanism, which enables a larger fraction of the available gain bandwidth to be utilized. However, this comes at the cost of an increased complexity in the resonator design, which couples resonator stability and pulse formation. This reduces the flexibility of KLM and makes initiating pulse formation more challenging.
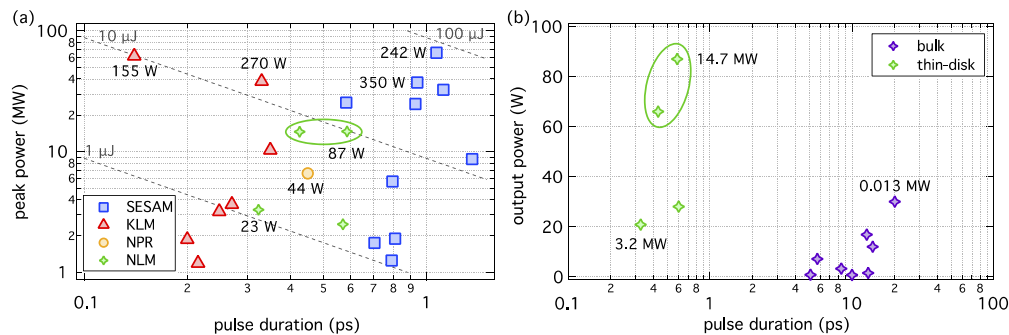

Fig. 1. (a) Overview of passively modelocked thin-disk laser results obtained with the gain material Yb:YAG and different modelocking techniques. References [18,19,24–37]. NPR: nonlinear polarization rotation [38]. The dashed lines indicate constant pulse energy values. The average power of state-of-the art results is indicated on the graph and the presented results are highlighted by the green circle. (b) Average output power and pulse duration of NLM-modelocked oscillators in the thin-disk and bulk geometries. References [21–23,39–43]. The peak power of state-of-the-art results is indicated on the graph and the presented results are encircled in green.

An attractive alternative providing a fast loss modulation is for example the frequency-doubling nonlinear-mirror (NLM) modelocking technique [20]. In this technique, the output coupler (OC) of the laser cavity is replaced with a new device: an intracavity $\chi^{(2)}$ crystal cut for type-1 second-harmonic generation (SHG), combined with a dichroic output coupler (OC) fully reflecting the second harmonic (SH) but only partially reflecting the fundamental wave (FW) [20]. The incident intracavity FW light is partly converted to the SH in the $\chi^{(2)}$ crystal, experiences losses at the dichroic OC, and is partially replenished by the fully reflected SH in the return pass through the $\chi^{(2)}$ crystal (described in Section 2.1 and Fig. 2). Since SHG is a nonlinear process, higher reflectivities are obtained at higher intensities, yielding a saturable loss mechanism [20]. The resulting NLM promises to combine the advantages of SESAM modelocking and KLM by providing a large, ultrafast, and absorption-free loss modulation that is decoupled from the

oscillator geometry. These features make NLM modelocking ideally suited to generate ultrashort pulses at high average powers.
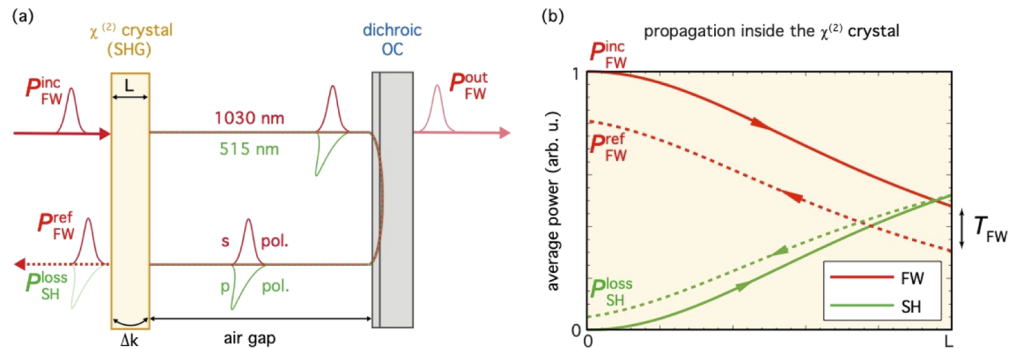

Fig. 2. Nonlinear mirror (NLM): (a) Operating principle of the NLM device: the incident fundamental wave (FW) at 1030 nm is partially converted to the second harmonic (SH) in the $\chi^{(2)}$ crystal, then experiences higher losses than the SH upon reflection on the dichroic output coupler (OC), and is finally replenished by the OPA process during the second propagation through the $\chi^{(2)}$ crystal. The phase-mismatch Δk and the air gap determine the efficiency of the second harmonic generation (SHG) process and the back-conversion, respectively. (b) Evolution of the power in the FW and SH during the first pass through the $\chi^{(2)}$ crystal leading to the generation of the SH (solid lines) and during the second pass through the crystal converting the energy back to the FW (dashed lines). T_{FW}: transmission of the dichroic OC for the FW.

NLM modelocking was mainly investigated with low-power, high repetition rate bulk oscillators. Due to the low available intracavity power, this required the use of few-millimeter-long $\chi^{(2)}$ crystals, which severely limited the lowest achievable pulse duration to >5 ps [21–23] (Fig. 1(b)) due to group-velocity mismatch (GVM) between the FW and SH in the $\chi^{(2)}$ crystal. The higher intracavity peak power available from thin-disk laser oscillators allows for the use of much thinner crystals ($\approx$1 mm), thereby enabling significantly shorter pulses. In our recent first demonstration of an NLM-modelocked thin-disk laser, we used a 0.5-mm-thick BBO crystal and obtained pulses as short as 323 fs at an average power of 21 W, reaching 3.2 MW of peak power [24] (Fig. 1(b)). It is worth noting that the achieved pulse duration is comparable to typical pulse durations obtained with KLM (Fig. 1(a)), and is the first sub-picosecond pulse duration reported for NLM-modelocking, to the best of our knowledge (Fig. 1(b)).

Here we demonstrate significant improvements in NLM-modelocked thin-disk lasers towards the state-of-the-art demonstrated with other modelocking techniques. We combine the fast loss modulation of the NLM with a SESAM to obtain a reliable initiation of pulsed operation and optimize the NLM-modelocking process in terms of Q-switching instabilities that arise in this new regime of laser operation (femtosecond NLM). We demonstrate an NLM-modelocked thin-disk laser delivering 66 W in 426-fs pulses at 9.3 MHz in a first configuration, and up to 87 W with 586-fs pulses at 8.8 MHz in a second configuration. The ultrafast oscillator produces pulses with energies up to 9.8 µJ and peak powers up to 14.7 MW (Fig. 1). In particular, we demonstrate peak powers in excess of 10 MW for the first time with an NLM-modelocked oscillator, while the average power is three times higher than previously demonstrated with this modelocking technique, to the best of our knowledge. Moreover, as illustrated in Fig. 1, the pulse duration is significantly shorter than typically achieved by high-power SESAM-modelocked Yb:YAG thin disk lasers.

In the following, we first present our modelocking results (section 2) and comment on our approach to mitigate Q-switching instabilities (section 3). In the final part we present our

investigation of the NLM-modelocking regime (section 4) and conclude with prospects for further power scaling.

2. High-power NLM-modelocked oscillator

In this section we present our high-power NLM-modelocked thin-disk laser. We took several key steps compared to our earlier result [24] to enable the improved performance:

(1) We used a state-of-the-art Yb-doped thin-disk module from TRUMPF.

(2) We implemented an active-multipass cavity geometry to optimize the oscillator for high-power operation and simultaneously lower the repetition rate compared to previous results.

(3) We improved the thermal and damage properties of the NLM device by using a low-absorption LBO crystal as the $\chi^{(2)}$ medium, and optimized dichroic output coupler (OC) coatings leading to a higher damage threshold.

(4) We included an intracavity SESAM to assist the optimization of the NLM device during modelocking and reliably initiate pulsed operation.

(5) We carefully characterized the NLM operating regime, allowing us to define guidelines to avoid Q-switching instabilities and tune the pulse duration during modelocked operation.

We first present the operating principles of the NLM device and introduce its tuning parameters, then describe the thin-disk oscillator and finally present the modelocking results.

2.1. NLM operating principle

Here we describe the three-stage operating principle of the frequency-doubling NLM and introduce the key parameters used to tune the NLM device, as illustrated in Fig. 2:

(1) An incident FW with a power $P_{\text{FW}}^{\text{inc}}$ generates a SH with an efficiency depending on the phase-mismatch $\Delta k = k_{\text{SH}} - 2k_{\text{FW}}$ (Fig. 2(b), solid lines).

(2) The FW and SH co-propagate to the OC where a part $P_{\text{FW}}^{\text{out}}$ of the FW is transmitted. The reflected FW and SH co-propagate back to the $\chi^{(2)}$ crystal. The waves accumulate a relative phase offset due to dispersion in the air gap and different reflection phases in the dichroic OC coating layers.

(3) The SH is converted back to the FW via optical-parametric amplification (OPA) (Fig. 2(b), dashed lines), resulting in a reflected power $P_{\text{FW}}^{\text{ref}}$ at the FW and a residual power loss $P_{\text{SH}}^{\text{loss}}$ in the SH. The efficiency of the back-conversion process is determined by the relative phase offset introduced by the difference in the refractive index of air for the FW and SH, and can be adjusted experimentally via the air gap.

As emerges from this description, for a given beam size on the $\chi^{(2)}$ crystal, the operation of the NLM is mainly determined by two parameters: the phase-mismatch Δk, given by the angle of incidence of the intracavity beam on the $\chi^{(2)}$ crystal, and the air gap between the $\chi^{(2)}$ crystal and the dichroic OC. The operation of the NLM can be characterized experimentally by carefully measuring $P_{\text{FW}}^{\text{inc}}$ and $P_{\text{SH}}^{\text{loss}}$ via leakages of intracavity mirrors in addition to $P_{\text{FW}}^{\text{out}}$. The effective

nonlinear reflectivity, effective nonlinear transmission and SH losses of the NLM are then calculated as follows:

$$R_{\text{eff}} = 1 - \frac{P_{\text{FW}}^{\text{out}} + P_{\text{SH}}^{\text{loss}}}{P_{\text{FW}}^{\text{inc}}} \tag{1}$$

$$T_{\text{eff}} = P_{\text{FW}}^{\text{out}} / P_{\text{FW}}^{\text{inc}} \tag{2}$$

$$L_{SH} = P_{\text{SH}}^{\text{loss}} / P_{\text{FW}}^{\text{inc}} \tag{3}$$

2.2. Thin-disk laser oscillator

The thin-disk laser oscillator used in our experiments is depicted in Fig. 3(a) and is based on an Yb-doped thin-disk module from TRUMPF Lasers GmbH. In our experiments, we used a pump laser with a central wavelength of 940 nm and up to 400 W of power with a beam diameter of 4.4 mm on the disk. Under these conditions, the diopter change due to thermal lensing of the disk is <0.1 m^{-1} which we measured with an interferometer. In order to optimize the laser resonator for high output power, we increase the available roundtrip-gain by increasing the number of passes of the intracavity laser beam through the disk via a re-imaging scheme [32]. With three reflections on the disk, our cavity supports laser operation with an OC transmission >40% (Fig. 3(c)). The multipass arrangement also significantly increases the cavity length, leading to repetition rates around 9 MHz. The cavity layout is shown in Fig. 3(a). In addition to the multipass arrangement, it includes a telescope extension at one end of the cavity to adjust the beam size on the NLM device from ≈290 μm to ≈400 μm (Fig. 3(b)).

We first characterized the performance of the laser in cw operation, i.e. without the $\chi^{(2)}$ crystal and the SESAM inside the cavity. As we expect the overall cavity losses to decrease during modelocked operation, we operated the laser at two different values of the OC transmission. We achieved up to 160 W of average output power with a linear 25% OC, and 99 W with a linear 45% OC, at a pump power of 355 W (Fig. 3(c)). This corresponds to an optical-to-optical efficiency of 45% and 28% respectively. We also characterized the beam quality in both cases and measured an M^2 <1.15, confirming that the beam is close to diffraction-limited. For the modelocking experiments we choose to use a large linear OC transmission around 40% to minimize the intracavity power. The power slope with a 25% OC confirms that the cavity behaves well for lower cavity losses and higher intracavity powers.

2.3. Modelocking experiments

Femtosecond thin-disk lasers are usually modelocked in the soliton modelocking regime and therefore rely on the balance of intracavity self-phase modulation (SPM) and dispersion for pulse shaping, and a saturable absorber to initiate and stabilize pulsed operation [13]. The re-imaging scheme implemented to increase the number of laser passes on the disk results in numerous intracavity foci (Fig. 3(b)), leading to a large SPM contribution from the intracavity air. We compensate this nonlinear phase with Gires-Tournois-Interferometer (GTI)-type dispersive mirrors inserted in the multipass arrangement (Fig. 3(a)). Accounting for the dispersion of the intracavity thin-film polarizer (TFP) introduced for polarization selection, and the optional addition of a −5000 fs^2 GTI mirror to the cavity, the total cavity dispersion amounts to either ≈-31,600 fs^2 or ≈-41,600 fs^2 per roundtrip. In order to facilitate the optimization of the NLM device and achieve reliable initiation of the modelocked operation, we introduce a SESAM at one end of the cavity. Using the approach of Ref. [44], we characterized the SESAM nonlinear reflectivity as a function of the incident pulse fluence and retrieved a saturation fluence of 35 μJ/cm^2, a modulation depth of 2.7%, nonsaturable losses of 0.35% and a rollover parameter of 0.5 J/cm^2 (for a pulse duration of 170 fs). The 1/e^2 intracavity beam radius on the SESAM is ≈950 μm.
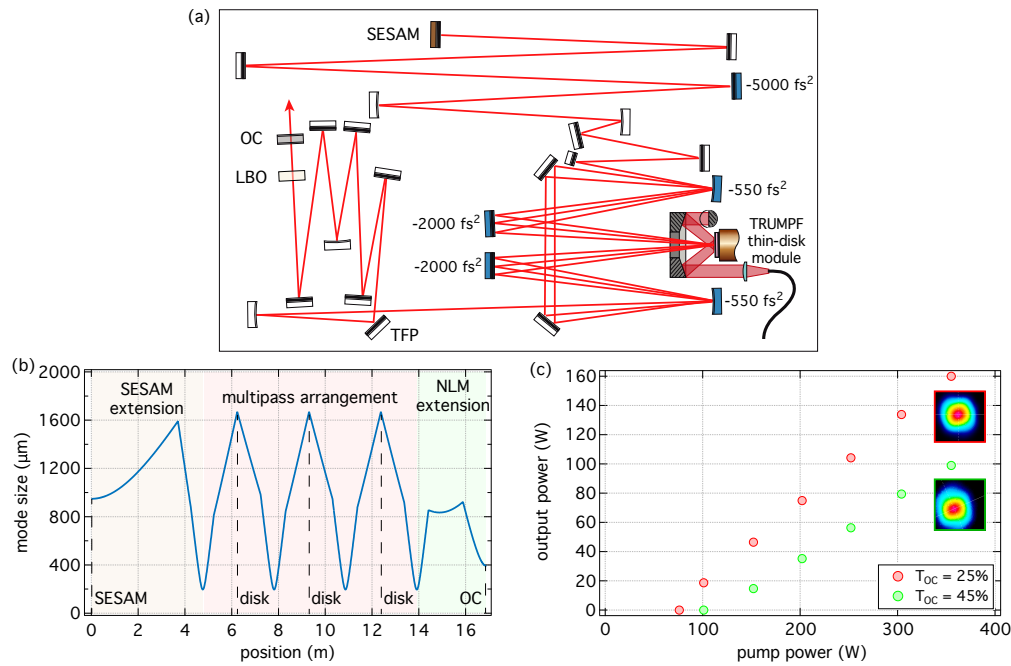
Fig. 3. SESAM-assisted NLM-modelocked thin-disk laser oscillator: (a) Cavity layout. The mirrors indicated with a blue color are Gires-Tournois-Interferometer (GTI)-type mirrors and introduce negative group delay dispersion (GDD). The multipass arrangement is extended on one end towards the SESAM and on the other end towards the NLM device. A thin-film polarizer (TFP) is introduced for polarization control. The multipass arrangement also includes most of the intracavity dispersion. (b) Evolution of the $1/e^2$ cavity mode radius. The re-imaging scheme on the disk leads to numerous foci. (c) Output power slopes in cw operation for two different OCs. The insets show the corresponding beam profiles at the highest power.

For our first modelocking experiments, we used a 0.5-mm-thick BBO crystal and a 45% dichroic OC for the NLM device. The $1/e^2$ intracavity beam radius on the BBO crystal was ≈290 μm. We operated the NLM at a non-zero SHG phase-mismatch Δk in order to mitigate Q-switching instabilities (see section 3). With an intracity dispersion of ≈-31,600 fs^2, we achieved up to 66 W of average output power with pulses as short as 426 fs full-width at half maximum (FWHM), at a repetition rate of 9.3 MHz (Figs. 4(a)–4(c)). This corresponds to a pulse energy of 7.1 μJ and a peak power of 14.7 MW. Using a leakage through one of the intracavity mirrors, we estimate the intracavity average power to be ≈180 W, corresponding to an effective transmission of the NLM device of ≈36.7% (Eq. (2)). We also measured the maximum temperature of the BBO crystal with a thermal camera and found that it exceeds 80 °C, which would ultimately limit power scaling [45]. The heat load on the crystal is likely due to linear absorption at the laser or second-harmonic wavelength. The linear absorption is specified by the manufacturer (EKSMA) as <1000 ppm/cm at 1030 nm. Additionally, the dichroic OC was very susceptible to damage when initiating modelocking.

To target higher powers, we therefore improved the thermal and damage properties of the NLM device. We replaced the BBO crystal by a low-absorption LBO crystal (<20 ppm/cm at 1030 nm, Cristal Laser) and designed an optimized dichroic coating for the OC mirror with high-damage threshold (see section 3). Furthermore, we increased the beam size on the LBO
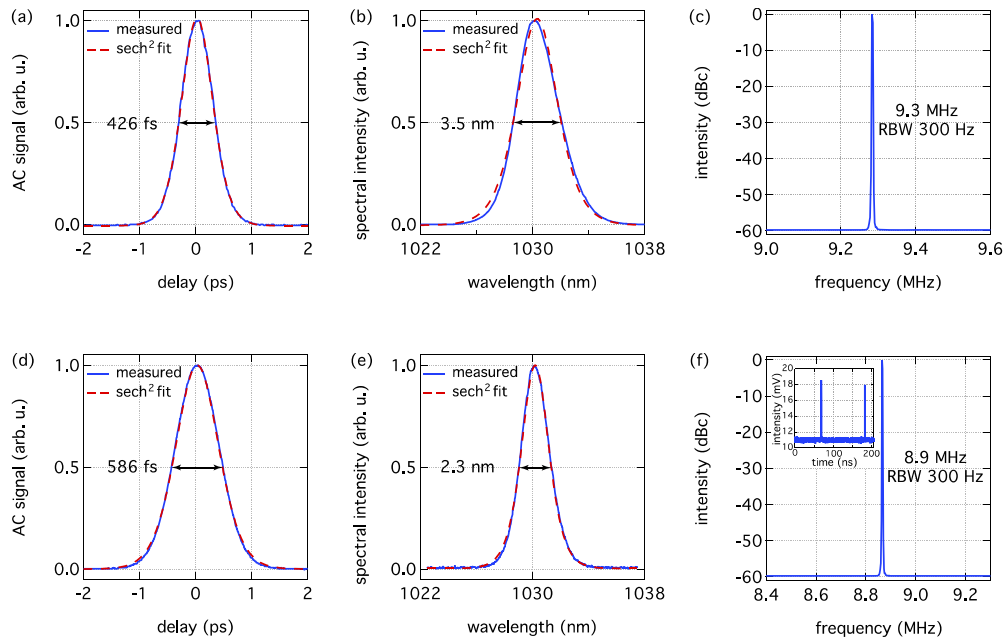
Fig. 4. High-power NLM-modelocked thin-disk laser oscillator: (a) Autocorrelation trace of the 426-fs pulses obtained at 66 W. (b) Optical spectrum of the 426-fs pulses, with a time-bandwidth product (TBP) of 1.34×0.315 (a transform-limited sech^2-pulse has 0.315). (c) Microwave spectrum analyzer (MSA) trace showing the repetition rate of 9.3 MHz. (d) Autocorrelation trace of the 586-fs pulses obtained at 87 W. (b) Optical spectrum of the 586-fs pulses, with a TBP of 1.21×0.315. (c) MSA trace showing the repetition rate of 8.9 MHz. The inset shows a sampling scope measurement with a 45-GHz fast photodiode. No side-pulse is apparent over the roundtrip time of 112.4 ns.

crystal to ≈400 µm, in order to saturate the NLM device at higher peak powers. Using a 1-mm-thick LBO and a 40% dichroic OC, and with ≈-41,600 fs^2 of intracavity dispersion, we achieved modelocking up to 87 W with a pulse duration of 586 fs and a repetition rate of 8.9 MHz (Figs. 4(d)–4(f)), corresponding to a pulse energy of 9.8 µJ and a peak power of 14.7 MW. In this configuration, no damage of the dichroic OC occurred and the LBO crystal stayed at a temperature <25 °C, for an intracavity power of ≈240 W. The effective transmission of the NLM device in that case was ≈36.3%. For both results, we verified that no double-pulse was present by scanning the autocorrelation delay over a range of ≈60 ps. Additionally, we measured the pulse train with a fast (45 GHz) photodiode and a sampling oscilloscope.

The results presented in this section show the power-scalability of the NLM modelocking technique towards the 100-W level. We improved the average power by a factor ≈3 over previous results while keeping femtosecond pulse durations and demonstrated peak powers close to 15 MW. Optimizing our oscillator also provided us with new insights into the mitigation of Q-switching instabilities and the influence of the NLM device on the pulse formation, which we present in the following section.

3. Study of the nonlinear-mirror modelocking regime

Here we describe the results of our investigation of the NLM-modelocking regime. In particular, we focus on avoiding Q-switching instabilities, which requires operation of the NLM device

with a finite phase-mismatch Δk. We carefully characterize the operation of the NLM in these conditions and show its influence on the shaping of the intracavity pulse.

3.1. Q-switching instabilities

The NLM provides a saturable nonlinear reflectivity for initiating and stabilizing pulsed operation [13]. However, unlike SESAM and KLM modelocking schemes, the NLM effectively saturates the reflectivity of the OC, i.e. the main contribution to the total cavity losses. On one hand, this enables a straightforward scaling of the available modulation depth by changing the OC transmission. On the other hand, however, this implies that the saturation of the NLM device strongly affects the Q-factor of the laser cavity (e.g. by potentially halving the cavity losses). As a result, NLM-modelocked lasers are susceptible to Q-switched modelocking instabilities with a strongly modulated amplitude of the pulse train.

The modulation depth provided by the NLM is maximized when operating the $\chi^{(2)}$ crystal at phase-matching $\Delta k = 0$, and adjusting the phase offset between the electric field of the SH and the electric field squared of the FW on the return pass to π (mod 2π) for optimal back-conversion (Fig. 5(a), blue curve) [24]. For short pulse durations, the group-velocity mismatch (GVM) between the FW and SH in the $\chi^{(2)}$ crystal leads to a reduction of the modulation depth, however this effect is small for the pulse durations considered here (>400 fs). In our experiments, we initially attempted to operate the NLM for optimal efficiency ($\Delta k = 0$ and optimal back-conversion), however we systematically damaged the dichroic OC due to Q-switching instabilities (Fig. 5(b)); the OC in this case was obtained commercially.

In the aftermath of these damage events, we fabricated a custom OC using ion-beam sputtering (IBS), designed to minimize the interaction of the SH with the coating layers. We designed this dichroic mirror to optimize the reflection of the SH within the first layers (see the green line in Fig. 5(c)) and adjusted the underlying layers for a flat 40% transmission of the FW and flat and nearly zero-dispersion for the FW and SH (Fig. 5(d)). We used SiO_2 as low- and Ta_2O_5 as high-index material. Since Ta_2O_5 has a bandgap of ~4.2 eV [46], two photon processes of the SH (about 2.4 eV) could ultimately limit further power scaling. Therefore we kept the field intensity of the SH (green line in Fig. 5(c)) low in the Ta_2O_5 layers. This resulted in a significantly improved damage threshold as no damage was observed with this mirror, despite continued Q-switched operation. If nonlinear effects or damage were a limiting factor for further power scaling, we could use HfO_2 (bandgap ~5.7 eV [47]) as a high-index material.

In order to mitigate Q-switching instabilities, we introduce a rollover in the nonlinear reflectivity curve of the NLM. The onset of rollover effects generally determine the transition between Q-switched modelocking and cw modelocking [48]. We detune the NLM from its optimal operation regime by rotating the $\chi^{(2)}$ crystal and changing the angle of incidence compared to phase-matching, and therefore operating at a finite phase-mismatch $\Delta k \neq 0$. This induces a rollover in the nonlinear reflectivity of the NLM that can be understood as follows: for a phase-matched cw interaction, the single-pass SHG process of the NLM does not exhibit back-conversion to the FW; however, with a finite phase-mismatch, back-conversion occurs after a certain distance through the SHG crystal, and the maximum SHG efficiency is reduced. Moreover, this distance decreases with input intensity and phase-mismatch [49]. In the context of an NLM device, these effects lead to a reduced maximum reflectivity and a rollover of the reflectivity at high intensities. Hence, the crystal phase mismatch can be used to limit both the available modulation depth and to reduce the intensity at which maximal reflectivity is obtained (Fig. 5(a), yellow and green curves).

By operating the NLM with a finite phase mismatch Δk, we suppressed Q-switching instabilities and achieved stable cw modelocking. Both results presented in section 2 were achieved in this regime, with a phase-mismatch $\Delta k < 0$. We further characterized the operation of the NLM in this regime, in particular its influence on pulse shaping.
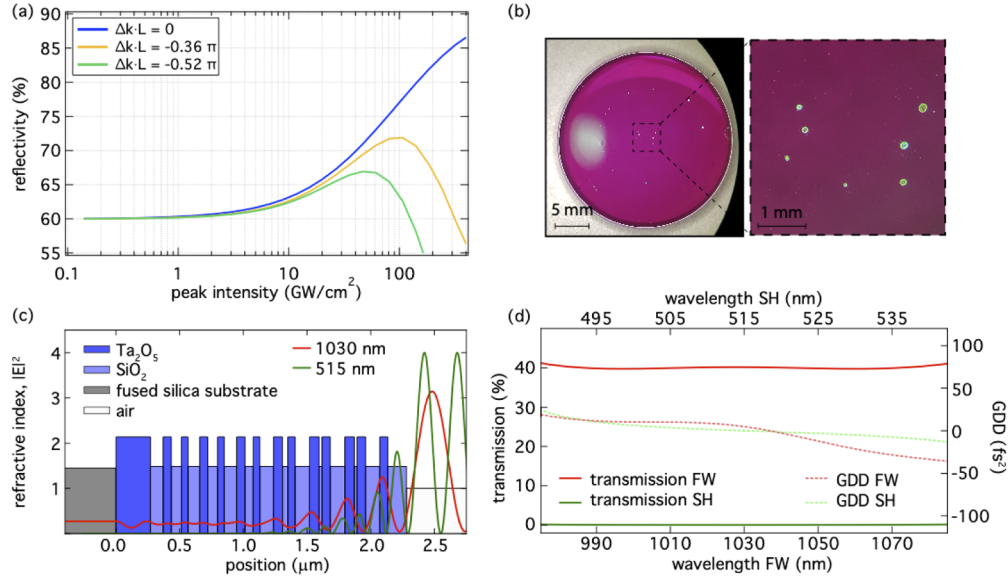
Fig. 5. Optimization of the NLM: (a) Simulated effective nonlinear reflectivity of the NLM device as a function of the incident pulse peak intensity for a 1-mm-long LBO and a 40% dichroic OC. The $1/e^2$ beam radius on the LBO is 300 μm and the pulse duration is set to 500 fs; the simulation assumes a Gaussian beam profile and a sech^2 pulse profile. The nonlinear reflectivity curve is plotted for different values of the phase mismatch Δk. For each case we adjust the phase offset between FW and SH to obtain an optimal back-conversion. (b) Microscope images of the OC mirror used in our first modelocking experiments at phase-matching $\Delta k = 0$, showing several damaged spots. (c) Custom-made dichroic OC using ion-beam sputtering (IBS). Layers and standing-wave pattern of the coating developed for increasing the damage-threshold of the dichroic OC. (d) Transmission and GDD of the produced dichroic mirror, shown for the FW and SH wavelengths.

3.2. Operation at non-zero phase-mismatch

In order to characterize the operation of the NLM, we carefully measure the output power at 1030 nm $P_{\mathrm{FW}}^{\mathrm{out}}$ directly with a power meter, as well as the incident power at 1030 nm $P_{\mathrm{FW}}^{\mathrm{inc}}$ and the SH loss power P_{SH}^{loss} from the NLM via leakages of intracavity mirrors. The experimentally deduced effective nonlinear reflectivity and SH losses of the NLM are then calculated using Eqs. (1) and (2). Furthermore, we estimate the nonlinear phase contribution of the NLM under the assumption of soliton modelocking [13].

The total roundtrip nonlinear phase contributing to the soliton pulse formation can be estimated using soliton theory [50]:

$$\varphi_{\mathrm{sol}} = -(1.76/\tau_{\mathrm{p}})^2 D_{\mathrm{rt}}, \tag{4}$$

where τ_{p} is the full-width at half-maximum (FWHM) pulse duration and D_{rt} is the total roundtrip dispersion. The two main sources of nonlinear phase-shifts contributing to the roundtrip B-integral B_{rt} are the NLM and the intracavity air. B_{rt} is the accumulated nonlinear phase for the peak of the pulse in space and time, and for free-space propagation the soliton phase φ_{sol} is related to B_{rt} via [51]:

$$\varphi_{\mathrm{sol}} = \frac{3}{4}B_{\mathrm{rt}} = \frac{3}{4}(B_{\mathrm{NLM}} + B_{\mathrm{air}}) = \varphi_{\mathrm{NLM}} + \varphi_{\mathrm{air}}, \tag{5}$$

where φ_{NLM} and φ_{air} are the effective roundtrip nonlinear phase contributions to the soliton pulse formation, accumulated in the NLM and the intracavity air respectively. The effective nonlinear

phase contribution from the intracavity air can be calculated using:

$$\varphi_{\mathrm{air}} = \frac{3}{4}B_{\mathrm{air}} = \frac{3}{4} \cdot \frac{2\pi}{\lambda}n_2^{\mathrm{air}} \int \frac{P_{\mathrm{pk}}}{\frac{\pi}{2}w(z)^2}dz, \tag{6}$$

where λ is the central wavelength of the pulse, n_2^{air} is the nonlinear refractive index of air, $w(z)$ is the $1/e^2$ intracavity beam radius, and P_{pk} is the pulse peak power. We deduce the nonlinear phase contribution from the NLM, under the assumption of soliton modelocking, by calculating: $\varphi_{\mathrm{NLM}} = \varphi_{\mathrm{sol}} - \varphi_{\mathrm{air}}$. We further define the SPM coefficients $\gamma_{\mathrm{NLM}} = \varphi_{\mathrm{NLM}}/P_{\mathrm{pk}}$ and $\gamma_{\mathrm{air}} = \varphi_{\mathrm{air}}/P_{\mathrm{pk}}$.

For our study, we use a 1-mm LBO and a 40% OC for the NLM. In cw operation, we initially align the LBO to obtain phase-matched SHG. The SH power generated in cw is of order 100 nW-1 μW and can be measured with a calibrated photodiode in order to optimize phase-matching. We then detune the angle of incidence by ≈20.7 mrad, corresponding to a phase-mismatch ΔkL = -0.61 π, similar to the detuning used in our modelocking experiments (L = 1 mm is the length of the LBO). Next, we optimize the air gap in cw operation to obtain optimal back-conversion of the SH to the FW. We then initiate modelocking by gently knocking the OC and tune the air gap in pulsed operation by moving the LBO to study the influence of the phase offset on the laser performance.

In Fig. 6(a), we show the evolution of the output power and the pulse duration as a function of the air gap. The first point of the scan (air gap ≈83 mm) corresponds to the optimal air gap for back-conversion in cw, with modelocked operation initiated at this point. We then translate the LBO away from the OC to increase the air gap. As observed on Fig. 6(a), the output power is ≈70 W and varies by less than 5% over the scan range. However, the pulse duration varies significantly over the same range, from ≈790 fs down to ≈490 fs, hinting towards a large change of the roundtrip nonlinear phase as a function of the air gap. Since the intracavity beam size on the LBO (predicted from ray transfer matrix calculations) stays virtually constant (310 ± 2 μm) across the scan range, the change in nonlinear phase can be attributed to the change of the NLM parameters, in this case the phase offset. Under the assumption of soliton shaping, we calculated the SPM coefficients $\gamma_{\mathrm{air}}, \gamma_{\mathrm{NLM}}$ for the intracavity air and for the NLM device and show the results in Fig. 6(c). The intracavity peak power was evaluated using $P_{\mathrm{pk}} = 0.88(P_{\mathrm{FW}}^{\mathrm{inc}}/f_{\mathrm{rep}})/\tau_{\mathrm{p,FTL}}$, where f_{rep} is the pulse repetition rate and $\tau_{\mathrm{p,FTL}}$ is the transform-limited pulse duration deduced from the measured spectrum of the output beam. As expected, the SPM coefficient for air is almost constant at ≈8 mrad/MW, as most of the SPM from air originates from the multipass part of the cavity, which essentially stays unaffected by the changing NLM air gap. The inferred SPM coefficient of the NLM device, however, varies significantly from ≈3.2 mrad/MW to ≈8.9 mrad/MW, becoming comparable to the SPM coefficient of the intracavity air for large air gaps. We conclude that the nonlinear phase introduced by the NLM is strongly dependent on the phase offset between the FW and SH on the return pass, and that this dependence leads to the tuning of the pulse duration we observe in Fig. 6(a). We have recently demonstrated compensation of positive SPM contributions with an intracavity phase-mismatched second-harmonic-generation crystal in a high-power thin-disk laser [52], which could be implemented to compensate or add to the nonlinear phase from the NLM device when targeting short pulses at higher powers and keep the laser operated in air.

We also calculated the experimental effective reflectivity and SH losses of the NLM device as a function of the air gap and plotted the results in Fig. 6(b). Interestingly, we initiated modelocking in a regime for which the effective reflectivity of the NLM is lower than the linear reflectivity of the OC, clearly indicating that the NLM device is not operating optimally. This indicates that the experimental conditions for optimal back-conversion in cw operation are different than those for pulsed operation, which could be due to a combination of intensity and temperature dependent
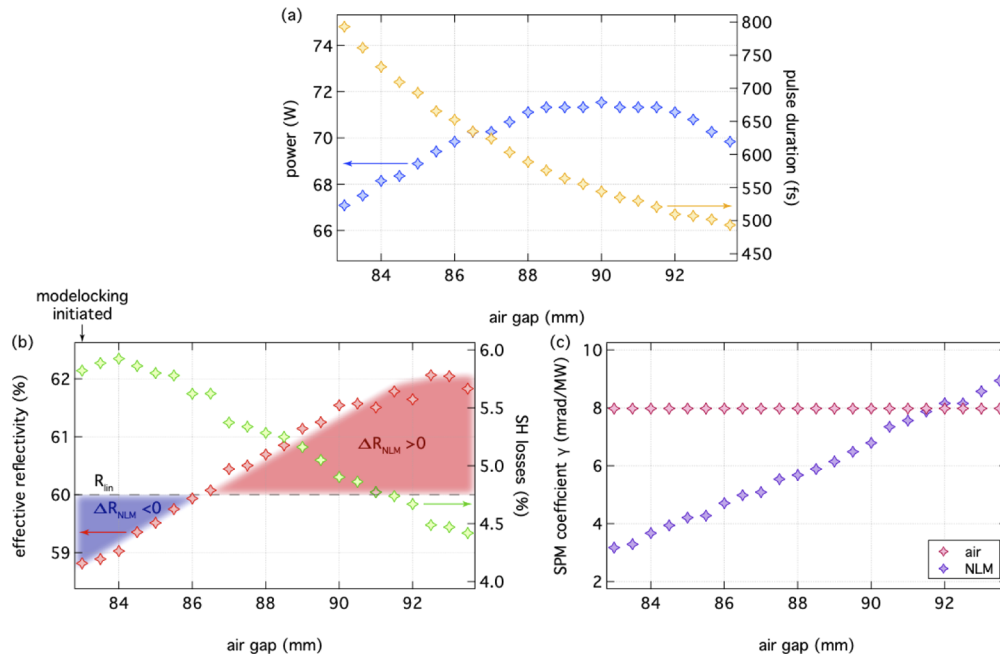
Fig. 6. Experimental characterization of the NLM-modelocking regime at a phase-mismatch $\Delta kL = -0.61\,\pi$. The NLM device combines a 1-mm LBO with a 40% dichroic OC. We tune the air gap in pulsed operation by moving the $\chi^{(2)}$ crystal relative to the OC. We show the evolution of: (a) the output power and pulse duration, (b) the experimentally deduced effective reflectivity and SH losses, the dashed line represents the linear reflectivity of 60%, (c) the deduced SPM coefficients for the intracavity air and the NLM device as a function of the air gap.

phase-shifts in the LBO crystal. This difference also justifies the presence of the SESAM in the cavity for initiating modelocking. We can differentiate two regimes of operation:

- Modelocking initiation: At the optimal air gap found in cw operation, we initiate modelocked operation. The SESAM losses are saturated, providing a modulation depth of $\approx 2\%$, but the NLM losses *increase* ($R_{\text{eff}} < R_{\text{lin}}$) by $\approx 1\%$, resulting in a net $\approx 1\%$ saturable loss in the cavity.

- Modelocking optimization: As we increase the air gap, the SESAM losses stay saturated, but the effective reflectivity of the NLM increases and eventually provides a net positive loss modulation (i.e. when $R_{\text{eff}} > R_{\text{lin}} = 60\%$) of $\approx 2\%$, resulting in a net 4% saturable loss in the cavity.

The fast loss modulation provided by the NLM supports the shorter pulses generated at larger air gaps. This improvement of the NLM operating regime when increasing the air gap is also reflected in the decreasing SH losses. It is worth noting that pulse durations <700 fs are usually not supported by SESAM-modelocked thin-disk lasers based on Yb:YAG [9,51], which further confirms the additional pulse reduction due to the fast saturable-absorber effect of the NLM device.

To summarize: we characterized the operation of the NLM device at a fixed phase-mismatch and variable air gap between the LBO crystal and the OC. By adjusting the air gap, we change the efficiency of the back-conversion process and hence the strength of the NLM. This tuning also yielded shorter pulses at the output of the oscillator. Based on the assumption of soliton pulse shaping, i.e. that the reduced pulse duration corresponds to a change in intracavity nonlinearity,

we deduce a strong dependence of the nonlinear phase contribution of the NLM on the phase offset set by the air gap.

3.3. Power scaling prospects

The underlying mechanism of the NLM is readily scalable by the beam size on the device. However, at some power level the thermal load on the crystal due to absorption at the FW or SH will become significant and lead to thermo-optic distortions. While thermal lensing effects are well-known in the context of power scaling, for an NLM there is the additional, related effect of thermal dephasing of the nonlinear interaction. Therefore, in this section we consider the sensitivity of the NLM process to changes in the phase mismatch, as would occur in the presence of excessive absorption in the crystal. We evaluate the case of an NLM consisting of a 1-mm-thick LBO crystal and a 40% dichroic OC, operating at a phase-mismatch $\Delta k.L = -0.36\pi$, for which the optimal peak intensity lies around 100 GW/cm^2 (Fig. 5(a), yellow). For a phase-mismatch $\Delta k.L = -0.52\pi$, the optimal peak intensity is reduced by a factor of two (Fig. 5(a), green). Using the temperature sensitivity of the phase mismatch of $d\Delta k/dT = 0.09 mm^{-1}/K$, calculated from the Sellmeier relations [53], we can evaluate the temperature difference leading to such a dephasing for a 1-mm LBO crystal and find a value of $\approx$5.6°C. Power scaling could most readily be achieved by finding a suitable crystal and beam geometry to keep the on-axis temperature increase (arising due to absorption at the FW and SH) below these levels. Given the multi-100-W SHG results achieved in recent years [7,52,54], we are optimistic about further power scaling of the NLM approach.

Additionally, shorter pulse durations could be generated by using GVM compensation techniques [22]. This could allow for the generation of sub-200 fs pulses from a multi-100 W NLM-modelocked TDL.

4. Conclusion and outlook

We presented a first power-scaled NLM-modelocked thin-disk laser oscillator delivering close to 15 MW of peak power in 426-fs or 586-fs pulses, representing a promising alternative to KLM for generating peak powers >10 MW at sub-500-fs pulse durations. We designed our laser resonator using a re-imaging scheme on the disk allowing us to couple out >40% of the intracavity power and operate at reduced repetition rates <10 MHz. We further used a SESAM to facilitate the optimization of the NLM device and enable reliable modelocked operation.

During our first modelocking attempts, we identified Q-switching instabilities as the main obstacle for stable cw modelocking because the NLM can saturate a large fraction of the cavity losses. We designed a new dichroic OC coating with a minimized interaction of the second harmonic wave and the coating layers, which led to significant improvements in terms of damage threshold. Furthermore, we mitigated Q-switching instabilities by operating the NLM device at a finite phase-mismatch, thus introducing a rollover in the nonlinear reflectivity of the device.

Using a BBO crystal, we demonstrated modelocking up to 66 W with 426-fs pulses at a repetition rate of 9.3 MHz. The crystal however suffered from a high absorption leading to a significant temperature increase during laser operation. For our next modelocking experiments, we replaced the BBO with a low-absorption LBO crystal and achieved up to 87 W of average power with a pulse duration of 586 fs and a repetition rate of 8.9 MHz. This is to the best of our knowledge the highest power demonstrated with the NLM-technique ($\approx$3 times more than the previous record [23]). The corresponding pulse energy is 9.8 μJ and the peak power is 14.7 MW.

We characterized the operation of the NLM device at a fixed phase-mismatch and in particular the influence of the phase offset on the laser performance. We tuned this parameter by adjusting the air gap between the $\chi^{(2)}$ crystal and the OC, which effectively adjusts the efficiency of the back-conversion process. This is confirmed by our experiments, showing an increase of the NLM reflectivity and a simultaneous decrease of the SH losses when tuning the air gap.

However, this tuning also significantly impacts the pulse formation process, likely due to a phase-offset-dependent nonlinear phase-shift provided by the NLM device. In our experiments, we could tune the pulse duration by a factor of almost two, from 790 fs down to 490 fs at almost constant output power. Based on this change and the other sources of nonlinear phase inside the cavity, we infer a change in the SPM coefficient introduced by the NLM device by one order of magnitude.

Our experiments validate the compatibility of the NLM for high-power modelocking. We expect that modelocking at multi-100s-W is achievable with the combination of low-absorption nonlinear crystals and optimized dichroic OC coating used in this work. Additionally, we identified a strong dependence of the NLM nonlinear phase on the tuning of the air gap, which can be exploited to tune the output pulse duration or calls for a strong intracavity source of SPM to decouple pulse shaping from NLM optimization. Finally, new NLM designs with a reduced loss modulation could allow for high-power NLM-modelocking at phase-matching without Q-switching instabilities.

Funding

Acknowledgments

Disclosures

The ETH Zurich authors signed an NDA with TRUMPF with regards to the thin-disk module and head.

References

1. U. Keller, "Recent developments in compact ultrafast lasers," Nature **424**(6950), 831–838 (2003).
2. T. Südmeyer, S. V. Marchese, S. Hashimoto, C. R. E. Baer, G. Gingras, B. Witzel, and U. Keller, "Femtosecond laser oscillators for high-field science," Nat. Photonics **2**(10), 599–604 (2008).
3. W. Sibbett, A. A. Lagatsky, and C. T. A. Brown, "The development and application of femtosecond laser systems," Opt. Express **20**(7), 6989–7001 (2012).
4. C. J. Saraceno, "Mode-locked thin-disk lasers and their potential application for high-power terahertz generation," J. Opt. **20**(4), 044010 (2018).
5. P. Russbueldt, T. Mans, J. Weitenberg, H. D. Hoffmann, and R. Poprawe, "Compact diode-pumped 1.1 kW Yb:YAG Innoslab femtosecond amplifier," Opt. Lett. **35**(24), 4169–4171 (2010).
6. M. Müller, A. Klenke, A. Steinkopff, H. Stark, A. Tünnermann, and J. Limpert, "3.5 kW coherently combined ultrafast fiber laser," Opt. Lett. **43**(24), 6037–6040 (2018).
7. J.-P. Negel, A. Loescher, A. Voss, D. Bauer, D. Sutter, A. Killi, M. A. Ahmed, and T. Graf, "Ultrafast thin-disk multipass laser amplifier delivering 1.4 kW (4.7 mJ, 1030 nm) average power converted to 820 W at 515 nm and 234 W at 343 nm," Opt. Express **23**(16), 21064–21077 (2015).
8. T. Nubbemeyer, M. Kaumanns, M. Ueffing, M. Gorjan, A. Alismail, H. Fattahi, J. Brons, O. Pronin, H. G. Barros, Z. Major, T. Metzger, D. Sutter, and F. Krausz, "1 kW, 200 mJ picosecond thin-disk laser system," Opt. Lett. **42**(7), 1381–1384 (2017).
9. C. J. Saraceno, F. Emaury, C. Schriber, A. Diebold, M. Hoffmann, M. Golling, T. Südmeyer, and U. Keller, "Toward Millijoule-Level High-Power Ultrafast Thin-Disk Oscillators," IEEE J. Sel. Top. Quantum Electron. **21**(1), 106–123 (2015).
10. A. Giesen, H. Hügel, A. Voss, K. Wittig, U. Brauch, and H. Opower, "Scalable concept for diode-pumped high-power solid-state lasers," Appl. Phys. B **58**(5), 365–372 (1994).

11. T. Gottwald, C. Stolzenburg, D. Bauer, J. Kleinbauer, V. Kuhn, T. Metzger, S. Schad, D. Sutter, and A. Killi, *Recent disk laser development at Trumpf*, SPIE Security + Defence (SPIE, 2012), Vol. 8547.

12. F. Saltarelli, I. J. Graumann, L. Lang, D. Bauer, C. R. Phillips, and U. Keller, "Power scaling of ultrafast oscillators: 350-W average-power sub-picosecond thin-disk laser," Opt. Express **27**(22), 31465–31474 (2019).

13. F. X. Kärtner, I. D. Jung, and U. Keller, "Soliton mode-locking with saturable absorbers," IEEE J. Sel. Top. Quantum Electron. **2**(3), 540–556 (1996).

14. F. X. Kärtner, J. A. D. Au, and U. Keller, "Mode-locking with slow and fast saturable absorbers-what's the difference?" IEEE J. Sel. Top. Quantum Electron. **4**(2), 159–168 (1998).

15. U. Keller, K. J. Weingarten, F. X. Kartner, D. Kopf, B. Braun, I. D. Jung, R. Fluck, C. Honninger, N. Matuschek, and J. A. D. Au, "Semiconductor saturable absorber mirrors (SESAM's) for femtosecond to nanosecond pulse generation in solid-state lasers," IEEE J. Sel. Top. Quantum Electron. **2**(3), 435–453 (1996).

16. C. J. Saraceno, C. Schriber, M. Mangold, M. Hoffmann, O. H. Heckl, C. R. E. Baer, M. Golling, T. Südmeyer, and U. Keller, "SESAMs for High-Power Oscillators: Design Guidelines and Damage Thresholds," IEEE J. Sel. Top. Quantum Electron. **18**(1), 29–41 (2012).

17. A. Diebold, T. Zengerle, C. G. E. Alfieri, C. Schriber, F. Emaury, M. Mangold, M. Hoffmann, C. J. Saraceno, M. Golling, D. Follman, G. D. Cole, M. Aspelmeyer, T. Südmeyer, and U. Keller, "Optimized SESAMs for kilowatt-level ultrafast lasers," Opt. Express **24**(10), 10512–10526 (2016).

18. J. Brons, V. Pervak, E. Fedulova, D. Bauer, D. Sutter, V. Kalashnikov, A. Apolonskiy, O. Pronin, and F. Krausz, "Energy scaling of Kerr-lens mode-locked thin-disk oscillators," Opt. Lett. **39**(22), 6442–6445 (2014).

19. J. Brons, V. Pervak, D. Bauer, D. Sutter, O. Pronin, and F. Krausz, "Powerful 100-fs-scale Kerr-lens mode-locked thin-disk oscillator," Opt. Lett. **41**(15), 3567–3570 (2016).

20. K. A. Stankov and J. Jethwa, "A new mode-locking technique using a nonlinear mirror," Opt. Commun. **66**(1), 41–46 (1988).

21. M. B. Danailov, G. Cerullo, V. Magni, D. Segala, and S. De Silvestri, "Nonlinear mirror mode locking of a cw Nd:YLF laser," Opt. Lett. **19**(11), 792–794 (1994).

22. G. Cerullo, V. Magni, and A. Monguzzi, "Group-velocity mismatch compensation in continuous-wave lasers mode locked by second-order nonlinearities," Opt. Lett. **20**(17), 1785–1787 (1995).

23. G. M. Thomas and M. J. Damzen, "30 W Nd:GdVO4 oscillator modelocked with nonlinear mirror," in *2011 Conference on Lasers and Electro-Optics Europe and 12th European Quantum Electronics Conference (CLEO EUROPE/EQEC)*, 2011), 1.

24. F. Saltarelli, A. Diebold, I. J. Graumann, C. R. Phillips, and U. Keller, "Modelocking of a thin-disk laser with the frequency-doubling nonlinear-mirror technique," Opt. Express **25**(19), 23254–23266 (2017).

25. O. Pronin, J. Brons, C. Grasse, V. Pervak, G. Boehm, M. C. Amann, V. L. Kalashnikov, A. Apolonski, and F. Krausz, "High-power 200 fs Kerr-lens mode-locked Yb:YAG thin-disk oscillator," Opt. Lett. **36**(24), 4746–4748 (2011).

26. J. Brons, O. Pronin, M. Seidel, V. Pervak, D. Bauer, D. Sutter, V. Kalashnikov, A. Apolonskiy, F. E. D. H. G. Krausz, and P. Moulton, "120 W, 4 µJ from a purely Kerr-lens mode-locked Yb:YAG thin-disk oscillator," in *Advanced Solid-State Lasers Congress*, OSA Technical Digest (online) (Optical Society of America, 2013), AF3A.4.

27. J. Zhang, J. Brons, N. Lilienfein, E. Fedulova, V. Pervak, D. Bauer, D. Sutter, Z. Wei, A. Apolonski, O. Pronin, and F. Krausz, "260-megahertz, megawatt-level thin-disk oscillator," Opt. Lett. **40**(8), 1627–1630 (2015).

28. J. Aus der Au, G. J. Spühler, T. Südmeyer, R. Paschotta, R. Hövel, M. Moser, S. Erhard, M. Karszewski, A. Giesen, and U. Keller, "16.2-W average power from a diode-pumped femtosecond Yb:YAG thin disk laser," Opt. Lett. **25**(11), 859–861 (2000).

29. E. Innerhofer, T. Südmeyer, F. Brunner, R. Häring, A. Aschwanden, R. Paschotta, C. Hönninger, M. Kumkar, and U. Keller, "60-W average power in 810-fs pulses from a thin-disk Yb:YAG laser," Opt. Lett. **28**(5), 367–369 (2003).

30. F. Brunner, E. Innerhofer, S. V. Marchese, T. Südmeyer, R. Paschotta, T. Usami, H. Ito, S. Kurimura, K. Kitamura, G. Arisholm, and U. Keller, "Powerful red-green-blue laser source pumped with a mode-locked thin disk laser," Opt. Lett. **29**(16), 1921–1923 (2004).

31. S. V. Marchese, T. Südmeyer, M. Golling, R. Grange, and U. Keller, "Pulse energy scaling to 5 µJ from a femtosecond thin disk laser," Opt. Lett. **31**(18), 2728–2730 (2006).

32. J. Neuhaus, J. Kleinbauer, A. Killi, S. Weiler, D. Sutter, and T. Dekorsy, "Passively mode-locked Yb:YAG thin-disk laser with pulse energies exceeding 13 µJ by use of an active multipass geometry," Opt. Lett. **33**(7), 726–728 (2008).

33. J. Neuhaus, D. Bauer, J. Zhang, A. Killi, J. Kleinbauer, M. Kumkar, S. Weiler, M. Guina, D. H. Sutter, and T. Dekorsy, "Subpicosecond thin-disk laser oscillator with pulse energies of up to 25.9 microjoules by use of an active multipass geometry," Opt. Express **16**(25), 20530–20539 (2008).

34. D. Bauer, I. Zawischa, D. H. Sutter, A. Killi, and T. Dekorsy, "Mode-locked Yb:YAG thin-disk oscillator with 41 µJ pulse energy at 145 W average infrared power and high power frequency conversion," Opt. Express **20**(9), 9698–9704 (2012).

35. C. J. Saraceno, F. Emaury, O. H. Heckl, C. R. E. Baer, M. Hoffmann, C. Schriber, M. Golling, T. Südmeyer, and U. Keller, "275 W average output power from a femtosecond thin disk oscillator operated in a vacuum environment," Opt. Express **20**(21), 23535–23541 (2012).

36. C. J. Saraceno, F. Emaury, C. Schriber, M. Hoffmann, M. Golling, T. Südmeyer, and U. Keller, "Ultrafast thin-disk laser with 80 µJ pulse energy and 242 W of average power," Opt. Lett. **39**(1), 9–12 (2014).

37. F. Saltarelli, I. J. Graumann, L. Lang, D. Bauer, C. R. Phillips, and U. Keller, "Power Scaling of Ultrafast Laser Oscillators: 350-W Output Power Sub-Ps SESAM-Modelocked Thin-Disk Laser," in *2019 Conference on Lasers and Electro-Optics (CLEO)*, 2019), 1–2.

38. B. Borchers, C. Schäfer, C. Fries, M. Larionov, and R. Knappe, "Nonlinear polarization rotation mode-locking via phase-mismatched type I SHG of a thin disk femtosecond laser," in *Advanced Solid State Lasers*, OSA Technical Digest (online) (Optical Society of America, 2015), ATh4A.9.

39. G. Cerullo, M. B. Danailov, S. De Silvestri, P. Laporta, V. Magni, D. Segala, and S. Taccheo, "A diode-pumped nonlinear mirror mode-locked Nd:YAG laser," Appl. Phys. Lett. **65**(19), 2392–2394 (1994).

40. P. K. Datta, Shivanand, S. Mukhopadhyay, A. Agnesi, and A. Lucca, "Picosecond pulse generation and its simulation in a nonlinear optical mirrormode-locked laser," Appl. Opt. **43**(11), 2347–2352 (2004).

41. G. M. Thomas, A. Bäuerle, D. J. Farrell, and M. J. Damzen, "Nonlinear mirror modelocking of a bounce geometry laser," Opt. Express **18**(12), 12663–12668 (2010).

42. G. M. Thomas, S. P. Chard, and M. J. Damzen, "High power modelocking of a stigmatic bounce geometry laser using a nonlinear mirror," Appl. Phys. B **101**(3), 553–557 (2010).

43. G. M. Thomas, T. Omatsu, and M. J. Damzen, "High-power neodymium-doped mixed vanadate bounce geometry laser, mode locked with nonlinear mirror," Appl. Phys. B **108**(1), 125–128 (2012).

44. D. J. H. C. Maas, B. Rudin, A. R. Bellancourt, D. Iwaniuk, S. V. Marchese, T. Südmeyer, and U. Keller, "High precision optical characterization of semiconductor saturable absorber mirrors," Opt. Express **16**(10), 7571–7579 (2008).

45. J. Rothhardt, S. Demmler, S. Hädrich, T. Peschel, J. Limpert, and A. Tünnermann, "Thermal effects in high average power optical parametric amplifiers," Opt. Lett. **38**(5), 763–765 (2013).

46. V. A. Shvets, V. S. Aliev, D. V. Gritsenko, S. S. Shaimeev, E. V. Fedosenko, S. V. Rykhlitski, V. V. Atuchin, V. A. Gritsenko, V. M. Tapilin, and H. Wong, "Electronic structure and charge transport properties of amorphous Ta2O5 films," J. Non-Cryst. Solids **354**(26), 3025–3033 (2008).

47. T. V. Perevalov, V. A. Gritsenko, S. B. Erenburg, A. M. Badalyan, H. Wong, and C. W. Kim, "Atomic and electronic structure of amorphous and crystalline hafnium oxide: X-ray photoelectron spectroscopy and density functional calculations," J. Appl. Phys. **101**(5), 053704 (2007).

48. T. R. Schibli, E. R. Thoen, F. X. Kärtner, and E. P. Ippen, "Suppression of Q-switched mode locking and break-up into multiple pulses by inverse saturable absorption," Appl. Phys. B **70**(S1), S41–S49 (2000).

49. R. Eckardt and J. Reintjes, "Phase matching limitations of high efficiency second harmonic generation," IEEE J. Quantum Electron. **20**(10), 1178–1187 (1984).

50. G. P. Agrawal, "Chapter 5 - Optical Solitons," in *Nonlinear Fiber Optics (Fifth Edition)* (Academic, 2013), pp. 129–191.

51. J. Herrmann, "Theory of Kerr-lens mode locking: role of self-focusing and radially varying gain," J. Opt. Soc. Am. B **11**(3), 498–512 (1994).

52. F. Saltarelli, A. Diebold, I. J. Graumann, C. R. Phillips, and U. Keller, "Self-phase modulation cancellation in a high-power ultrafast thin-disk laser oscillator," Optica **5**(12), 1603–1606 (2018).

53. K. Kato, "Temperature-tuned 90 deg phase-matching properties of LiB3/O5," IEEE J. Quantum Electron. **30**(12), 2950–2952 (1994).

54. T. Dietrich, S. Piehler, M. Rumpel, P. Villeval, D. Lupinski, M. Abdou-Ahmed, and T. Graf, "Highly-efficient continuous-wave intra-cavity frequency-doubled Yb:LuAG thin-disk laser with 1 kW of output power," Opt. Express **25**(5), 4917–4925 (2017).